Journal of Materials Chemistry A

ROYAL SOCIETY OF CHEMISTRY

PAPER

View Article Online
View Journal

Cite this: DOI: 10.1039/d5ta10161a

Micropore engineering of biomass-derived carbon for durable, high-loading aqueous all-organic pouch batteries

Keisho Ri, [ab] Nagihiro Haba, [ab] Ryotaro Kumashiro,[c] Ayaka Kido,[ab] Tomoya Yamada,[d] Yuto Katsuyama, [e] Masaru Watanabe,[d] Kayoko Kobayashi [f] and Yuta Nakayasu *[adg]

Aqueous all-organic batteries based on low-molecular-weight quinones are promising candidates for sustainable energy storage. However, their performance is limited by incomplete utilization of the monomers within porous carbon hosts and further deteriorates upon scaling to practical device formats. Here, we demonstrate that molecule-specific pore-structure design in biomass-derived activated carbons (ACs) enables a high-loading aqueous all-organic pouch cell with thick-film electrodes (areal active-material loading ≈28 mg cm^{-2}, areal energy density of ≈1 mWh cm^{-2}), delivering an energy density of 17.3 Wh kg^{-1} at 0.1C and retaining 99.75% of its capacity after 3000 cycles. These performance and durability metrics compare favorably with previously reported aqueous all-organic batteries at high areal loading and are consistent with the sealed, low-electrolyte pouch configuration and micropore confinement, which together suppress dissolution-based degradation. To rationalize these device-level gains, we developed design principles for biomass-derived AC hosts and evaluated their applicability in the fabrication of high-loading aqueous all-organic pouch cells. Pore analysis revealed distinct governing factors for the two quinones. While both primarily occupy 0.7–0.8 nm micropores, tetrachloro-1,4-benzoquinone (TCBQ) utilization is facilitated by the presence of a mesopore network; accordingly, in carbons lacking mesopores, diffusion limitations lead to significantly suppressed TCBQ utilization. In contrast, 1,5-dichloroanthraquinone utilization is determined by the 0.7–0.8 nm micropore volume and suffers from a molecular sieving effect in low-surface-area carbons, where constricted pore entrances exclude the molecule. This work demonstrates that rational, molecule-specific design of biomass-derived ACs can translate nanoscale confinement principles into practical device-level gains, paving the way for durable and sustainable energy storage.

Received 12th December 2025
Accepted 20th March 2026

DOI: 10.1039/d5ta10161a

rsc.li/materials-a

Introduction

The transition toward sustainable energy requires high-performance, safe, and environmentally benign energy storage systems.[1,2] Aqueous all-organic batteries based on small-molecule redox-active species have recently emerged as attractive candidates because they offer intrinsic safety while using earth-abundant, metal-free active materials – thereby ensuring broad resource availability.[3–5] Organic electrode materials fall into two broad classes: polymers and low-molecular-weight (LMW) compounds. Redox-active polymers exhibit low solubility in electrolytes, which suppresses dissolution of the active species and thereby improves capacity retention and cycling stability. However, they often suffer from low theoretical capacities, slow reaction kinetics, and complex synthesis routes.[6] LMW organic molecules, particularly quinones, are a compelling alternative because of their wide accessibility and facile synthesis under mild conditions.[7–9] Furthermore, LMW quinones exhibit high theoretical capacities (*e.g.*, >400 mA h g^{-1} for some derivatives[10]), fast redox kinetics, and exceptional design flexibility that allows the precise tuning of their properties *via* molecular engineering.[11] However, their application faces practical challenges owing to their low intrinsic electronic

[a]*Frontier Research Institute for Interdisciplinary Sciences, Tohoku University, 6-3 Aoba, Aza, Aramaki, Aoba-ku, Sendai, Miyagi 980-8578, Japan. E-mail: nakayasu@tohoku.ac.jp*

[b]*School of Engineering, Tohoku University, 6-6 Aoba, Aza, Aramaki, Aoba-ku, Sendai, Miyagi 980-8579, Japan*

[c]*Advanced Institute for Material Research, Tohoku University, Sendai 980-8577, Japan*

[d]*Research Center of Supercritical Fluid Technology, Graduate School of Engineering Tohoku University 6-6-11, Aoba, Aza, Aramaki, Aoba-ku, Sendai, Miyagi 980-8579, Japan*

[e]*Department of Chemistry & Biochemistry, University of California Los Angeles, Los Angeles, California, 90095-1569, USA*

[f]*Division of Forest and Biomaterials Science, Graduate School of Agriculture, Kyoto University, Sakyo-ku, Kyoto 606-8502, Japan*

[g]*Satoyama Engineering Co., Ltd, Matsubamoriyama 25-8, Maekawa, Shibata Gun Kawasaki Machi, Miyagi 989-1501, Japan*

conductivity and high solubility in aqueous electrolytes.[12–15] In particular, high solubility leads to active material crossover and rapid capacity degradation, which reduces the durability of aqueous all-organic batteries.

A proven strategy to overcome these issues is to confine the active molecules within the nanopores of a conductive carbon host.[15–19] Activated carbons (ACs) are ideal hosts owing to their low cost, robust stability, high surface area, and tunable porosity.[20,21] Recent reviews have also highlighted that engineering a hierarchical pore structure is crucial for maximizing the performance of biomass-derived carbon materials.[22] Moreover, biomass-derived ACs produced from agricultural or forestry residues are increasingly recognized as environmentally advantageous, as life cycle assessments generally report that they have lower climate impacts than petroleum-derived carbons owing to renewable feedstocks and the utilization of waste streams.[23–25]

Maxsorb® (a petroleum-coke-derived AC) has been widely used as a high-performance benchmark, but biomass-derived ACs offer a more sustainable and cost-effective alternative with diverse, tunable porosity. In our previous work, an AC made from high-quality oak wood proved to be highly conductive and enabled ~97.6% utilization of anthraquinone.[16] However, this success did not extend to all active materials: in the same optimized system, another quinone (*p*-chloranil) achieved only about 75% utilization.[17,18,26] Achieving high utilization for more economical and widely available biomass ACs has also proven difficult, with many studies reporting limited redox capacity due to suboptimal pore structures or low conductivity.[16,17,27–29] A critical question is whether structurally distinct active materials require the same host optimization strategy, or whether their differing molecular geometries and association tendencies necessitate distinct host properties. We hypothesized that each quinone would demand a tailored pore structure for optimal utilization–in other words, tetrachloro-1,4-benzoquinone (TCBQ, a benzoquinone derivative) and 1,5-dichloroanthraquinone (DCAQ, an anthraquinone derivative) may benefit from different pore size distributions and connectivity.

Recent aqueous organic and rocking-chair-type dual-organic proton cells have achieved gravimetric energy densities in the range of 14–60 Wh kg^{-1}, albeit at relatively low areal loadings (≈1–10 mg cm^{-2}) and/or in small-area cell formats based on highly graphitized carbons and specialized architectures.[18,30,31] In such systems, the areal energy density at low rates is often limited to ~0.3–0.8 mWh cm^{-2}. Additionally, many aqueous organic systems still suffer from rapid capacity decay, with capacity losses of ~15% over 100 cycles and up to ~30–40% over 1000 cycles being commonly reported.[17,32] Thus, translating high gravimetric performance into practical, thick-electrode pouch cells using widely available biomass-derived ACs, while simultaneously maintaining long-term stability, remains a key challenge for aqueous all-organic devices.

Herein, we established molecule-specific design principles for TCBQ and DCAQ by elucidating the distinct roles of pore accessibility and micropore confinement in determining their redox capacities. Guided by these hierarchical pore design principles, we successfully translated them into a practical high-loading pouch cell with exceptional long-term stability. Detailed analysis revealed that TCBQ utilization is facilitated by the mesopore network and is comparatively tolerant of variations in pore structure. In contrast, DCAQ utilization is strongly influenced by the availability of 0.7–0.8 nm micropores and is highly sensitive to molecular sieving effects, requiring high-surface-area hosts to ensure accessibility. High-*q* wide-angle X-ray scattering (WAXS) further suggests possible differences in the local short-range scattering response under confinement, but this information is used only as complementary, hypothesis-generating evidence.

Based on these distinct design principles, we constructed an optimized and practical-sized full pouch cell using a selected, low-cost biomass-derived AC host. The pouch cell employed thick-film electrodes with an areal active material loading of ≈28 mg cm^{-2}, corresponding to an areal energy density of ≈1 mWh cm^{-2} at 0.1C. The device achieved a gravimetric energy density of 17.3 Wh kg^{-1} at 0.1C and retained 99.75% of its capacity after 3000 high-rate cycles, corresponding to ~0.25% capacity fade over 3000 cycles. These results indicate stable long-term operation under high-loading and high-rate conditions and compare favorably with previously reported large-format aqueous all-organic devices.

Results and discussion

To address this hypothesis, we systematically examined a set of biomass-derived AC hosts with varying pore structures to elucidate how pore accessibility and micropore confinement distinctly impact the redox capacities of TCBQ and DCAQ. Based on these findings, we then constructed a practical high-loading pouch cell to validate that the optimized, molecule-specific pore design indeed yields exceptional long-term performance.

Design principles for optimized AC

Seven types of commercial biomass-derived ACs, as well as Maxsorb® derived from petroleum coke and pitch (abbreviated as "Max" in all figures and tables), were prepared. First, the electrical resistances (from conductivity measurements) and specific surface areas (SSAs, from N_2 adsorption–desorption isotherms) of the pristine AC host materials were determined. Additionally, the loading amounts and redox capacities of the TCBQ and DCAQ monomers were measured. These values are summarized in Table 1, and representative galvanostatic charge–discharge curves and combustion ion chromatography data used to derive the redox capacities and loading amounts are provided in Section S1 of the SI.

The ACs exhibited high SSA values, with those of samples 1 and 2 approaching 2000 m^2 g^{-1}. For comparison, in electric double-layer capacitors (EDLCs), the capacitance often plateaus once the SSA approaches this range, a behavior commonly attributed to the presence of micropores that are too small to be accessible to electrolyte ions, which contribute to the measured SSA but not to ion adsorption.[33]

Electronic conductivity was identified as a critical factor in our system. Between samples 5 and 7, which possess nearly

Table 1 Electrical conductivities and specific surface areas (SSAs) of ACs, loading ratios of quinone monomers, and specific capacities and utilization rates of quinone monomers obtained from charge–discharge measurements

Sample	Ingredient	Activation method	Resistance (Ω cm)	SSA ($m^2\ g^{-1}$)	TCBQ loading (wt%)	TCBQ capacity (mA h g^{-1})	TCBQ utilization (%)	DCAQ loading (wt%)	DCAQ capacity (mA h g^{-1})	DCAQ utilization (%)
1	Coconut shell	H_3PO_4	36.6	1977	25.9	208	95.4	28.8	191	98.5
2	Coconut shell	Multi-step	21.6	1899	26.0	202	92.7	27.3	182	93.8
3	Wood	H_3PO_4	33.8	677	29.4	177	81.2	34.3	77	39.7
4	Cedar	Steam	43.1	652	25.9	154	70.6	27.3	96	49.5
5	Coconut shell	Steam	37.7	1375	27.7	180	82.6	27.7	162	83.5
6	Wood	H_3PO_4	N.D.	1360	15.8	0	0.0	31.6	0	0.0
7	Cedar	Alkaline	N.D.	1411	22.5	0	0.0	29.2	0	0.0
Max	Petroleum coke	Alkaline	17.0	3100	25.9	206	94.5	28.8	193	99.5

identical SSA values and monomer loading, only the more conductive sample 5 exhibited any redox capacity, highlighting that sufficient electronic transport is indispensable.[34,35] Therefore, the non-conductive samples (6 and 7) were excluded from further analysis, and subsequent correlation analyses focused on the conductive biomass-derived ACs (samples 1–5). All coefficients of determination reported below refer to adjusted R^2 (Adj. R^2) values obtained by linear regression.

Within this conductive sample group, the redox capacities generally followed the trend of SSA (Fig. 1a and b). However, the correlation was not strictly linear. Specific deviations, such as the suppressed capacity of the high-SSA sample 5 in TCBQ, suggest that the total BET surface area is not the sole determinant of performance. It is established that electrochemical performance is governed by the accessible surface area available to electrolyte ions and active molecules rather than the total surface area.[36] Therefore, to elucidate the distinct structural factors governing the utilization of TCBQ and DCAQ beyond simple surface area, we proceeded to analyze the specific pore architectures and their interaction with molecular dimensions.

Correlation between micropore structure and redox capacity

Pore size distribution (PSD) analysis of the pristine AC hosts, derived from CO_2 adsorption isotherms, is provided in the SI (Fig. S2). Maxsorb® has a considerably larger micropore volume in the upper subnanometer range (≈0.8–1.0 nm and above) than the biomass-derived ACs, whereas the pore volumes of all samples are relatively similar at approximately 0.6 nm. This indicates that the superior performance of Maxsorb® cannot be attributed simply to a uniformly higher micropore volume across the entire subnanometer region, but rather to the distribution of pore volume within specific windows.

More detailed analysis revealed a fundamental divergence in the governing factors for the two quinones. For TCBQ, a strong linear correlation ($R^2 = 0.94$) between redox capacity and the 0.7–0.8 nm micropore volume was observed for samples 1, 2, and 4. This aligns with the principle that capacitance maximizes when pore size matches ion dimensions.[33,37,38] Indeed, the density functional theory (DFT)-optimized geometry of TCBQ (Fig. 2c) exhibits a short-axis dimension of 0.843 nm, suggesting a tight fit within the 0.7–0.8 nm micropores that enables effective confinement. However, deviations in samples 3 and 5 highlight the critical role of the mesopore network in the molecular impregnation process. To clarify the structural origins, the mesopore size distributions (Fig. S3) were compared with the micropore data (Fig. S2). Sample 5, prepared *via* steam activation, possesses abundant micropores but lacks mesopores. This structure is characteristic of steam activation, where moderate surface reactions primarily generate micropores without effectively broadening them into transport channels.[39] Consequently, sample 5 exhibited a suppressed capacity falling below the trend line (labeled lower in Fig. 2a). This suggests that the lack of mesopores hinders the diffusion of bulky TCBQ molecules into the deep microporous matrix during the impregnation step, leading to incomplete penetration into the internal microporous network and reduced

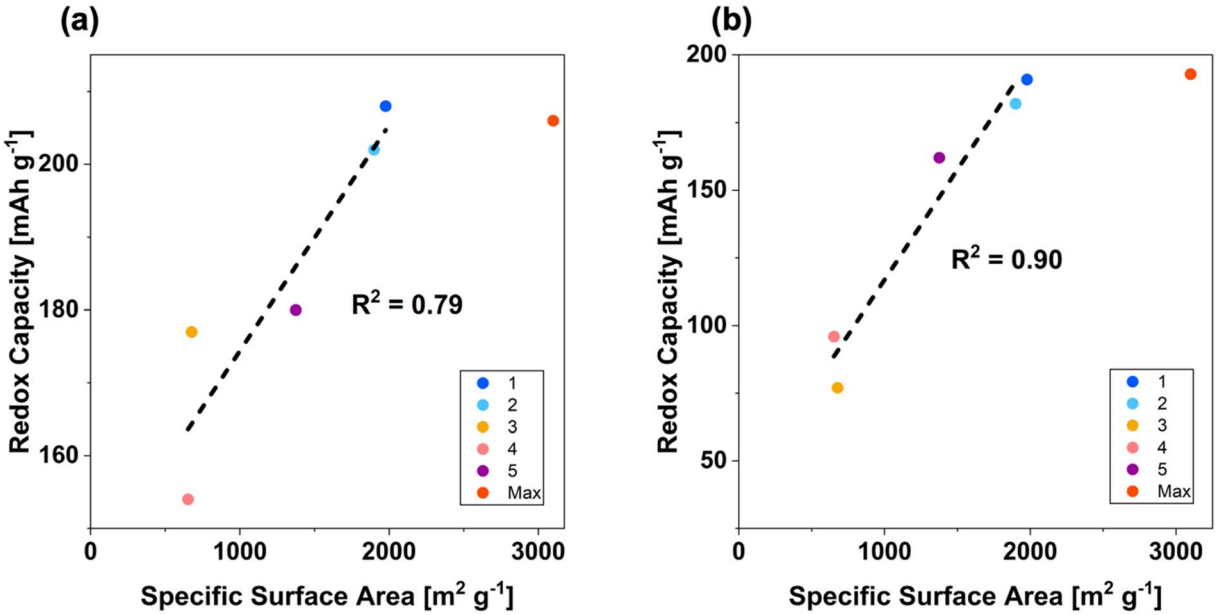

Fig. 1 Correlation between specific surface area and redox capacity for (a) TCBQ and (b) DCAQ. (The dashed lines indicate linear fits. All R^2 values represent adjusted coefficients of determination (Adj. R^2), unless otherwise noted.).

utilization of electrochemically relevant sites. In contrast, sample 3, prepared *via* chemical activation, possesses a developed mesopore network despite its significantly lower micropore volume. Chemical activation agents, such as phosphoric acid, promote mesoporosity *via* crosslinking and expansion of the carbon matrix.[40] This mesoporous network acts as a molecular highway, facilitating the mass transport of TCBQ molecules to access and uniformly fill the limited storage sites, allowing sample 3 to maintain a capacity comparable to sample 5 (labeled higher in Fig. 2a). Furthermore, it has been demonstrated that mesopores facilitate proton and ion transport within quinone-confined carbon networks, thereby enhancing utilization efficiency.[29,41] Thus, the mesopore network plays a dual role in ensuring both molecular accessibility during synthesis and ionic accessibility during operation. Consequently, TCBQ utilization is not solely determined by storage sites but is significantly facilitated by mesopore accessibility.

In contrast, DCAQ capacity showed a remarkable linear correlation ($R^2 = 0.94$) with the 0.7–0.8 nm micropore volume across all biomass-derived samples (samples 1–5). This indicates that DCAQ utilization is strongly confinement-controlled, scaling linearly with the number of available 0.7–0.8 nm storage sites regardless of the mesopore network development. In sample 3, the capacity was low (~77 mA h g^{-1}) simply because the specific pore volume was low, tracking the trend line perfectly. Unlike TCBQ, DCAQ does not benefit from mesopore-assisted transport if the specific storage sites are missing. This strict volume dependence corroborates the DFT-derived molecular size of DCAQ (0.970 nm, Fig. 2d). Furthermore, such micropore confinement is a prerequisite for activating the redox reaction of insulating organic solids; without this precise fit, the charge transfer resistance remains prohibitively high, resulting in negligible utilization.[42] Additionally, the capacity drop in low-surface-area hosts evidences a molecular sieving effect,[43] where constricted pore entrances physically exclude the larger molecules. It is established that electrochemical performance is ultimately governed by the accessible surface area.[36] Thus, while TCBQ allows for greater structural flexibility assisted by mesopores, DCAQ depends more strongly on the availability of appropriately sized micropore volume for high utilization.

However, CO_2-PSD cannot directly provide static structural information, such as which pores are filled to what extent, or what arrangements and aggregation states the monomers adopt within the pores.

Small-angle X-ray scattering (SAXS)/wide-angle X-ray scattering (WAXS) analysis of quinone-impregnated AC

To identify the key structural parameters governing the redox capacity, we analyzed the WAXS patterns in the high-q region, which probes short real-space length scales relevant to sub-nanometer electron-density fluctuations. In quinone-impregnated ACs, the micropores (<2 nm) may contain a heterogeneous mixture of carbon walls, impregnated organic molecules, and residual void, creating characteristic short-range electron-density contrast; therefore, changes in the high-q scattering feature can serve as a sensitive proxy for micropore-scale structural correlations associated with quinone confinement.

Because a rigorously defined Guinier regime could not be identified in the present high-q data, we do not apply Guinier analysis for absolute size determination. Instead, a Guinier-type linearization was used only as a phenomenological parameterization of the decay of a broad high-q scattering feature within a fixed q-window. The derived quantity d is treated as an apparent descriptor of the high-q profile shape for within-series comparison under an identical analysis protocol. It is not

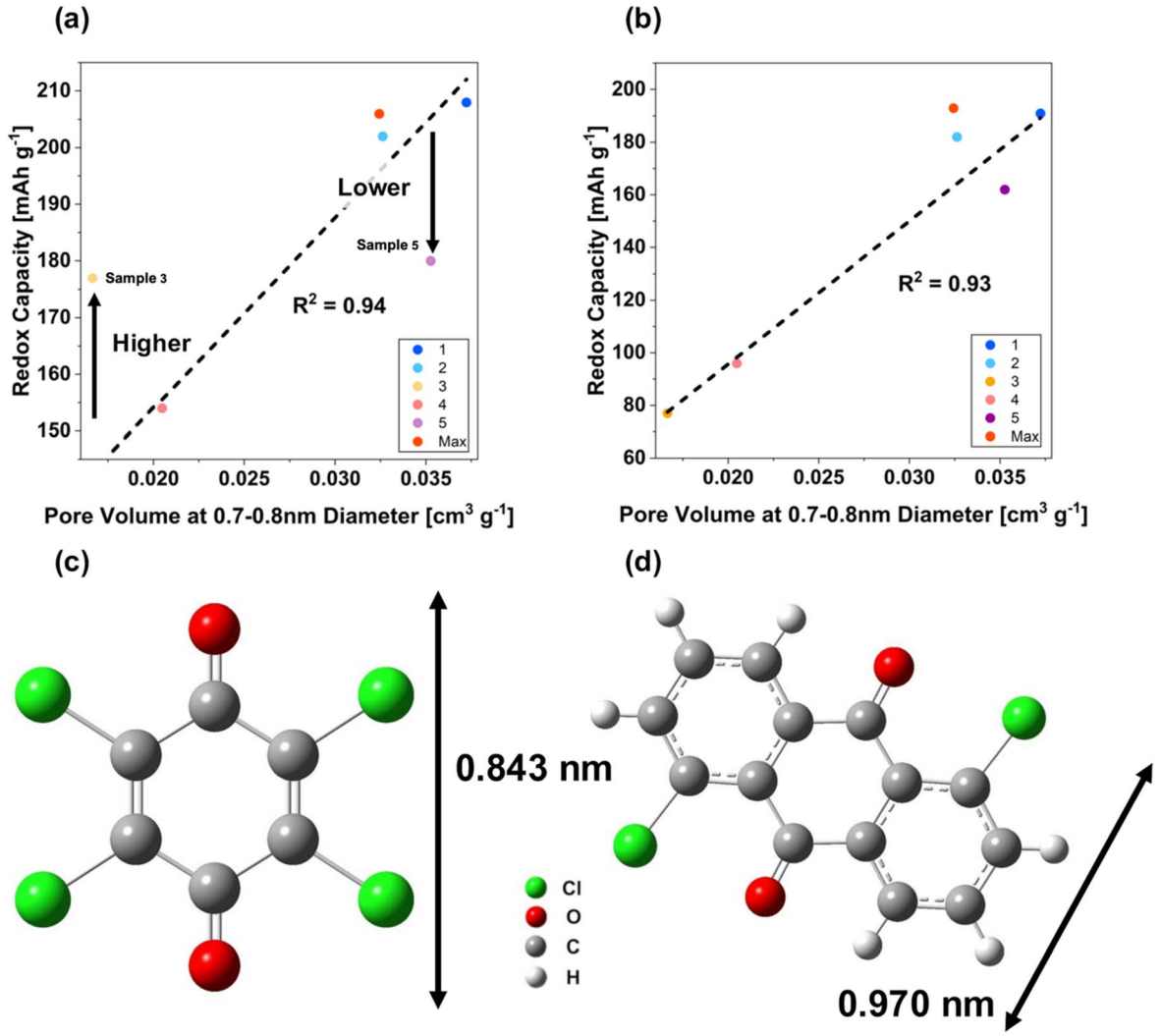

Fig. 2 Structure–performance correlation for TCBQ and DCAQ. Redox capacity as a function of the micropore volume at 0.7–0.8 nm (derived from CO_2-PSD) for (a) TCBQ and (b) DCAQ. DFT-optimized molecular structures of (c) TCBQ ($C_6Cl_4O_2$) and (d) DCAQ ($C_{14}H_6Cl_2O_2$), with the effective molecular diameter indicated. Detailed molecular dimensions, including short/long axes and thickness, are summarized in Table S3. The fitting line in (a) was obtained excluding samples 3 and 5.

interpreted as a pore diameter, a geometry-specific structural size, or any physically rigorous size parameter.[44,45] Specifically, we plotted ln $I(q)$ *vs.* q^2 over a fixed q-window and performed a linear fit to obtain an apparent fitting parameter, R_{app}, which was converted to d. Because ACs exhibit structurally heterogeneous, non-spherical pore networks and the high-q background can limit the appearance of an ideal Guinier regime, we do not interpret d as a gas-sorption pore diameter nor as evidence of a specific pore geometry. Rather, d is used only as an apparent descriptor of the high-q profile shape under a consistent fitting protocol, and its role is restricted to qualitative within-series comparison rather than structural assignment.

d-redox capacity relationship for TCBQ-impregnated electrodes and monomer filling state

For TCBQ, no monotonic relationship between d and redox capacity was observed (Fig. 3a). The broad scatter among lower-capacity samples indicates that this apparent high-q descriptor is influenced by multiple sources of heterogeneity and cannot by itself resolve the filling state of TCBQ. At most, the clustering of several higher-capacity samples at lower d is consistent with, but does not establish, a less heterogeneous local scattering response in better-performing samples. We therefore use d in the TCBQ series only as supplementary, non-predictive information and do not assign a unique structural origin to the observed scatter.

d-redox capacity correlation for DCAQ-impregnated electrodes and possible local association states

For DCAQ, larger d values coincided with higher redox capacity within the present dataset (Fig. 3b). Because a strict Guinier regime is not established, d is not interpreted as a quantitative domain size. Instead, the observed d-capacity relation is treated only as phenomenological, complementary evidence that the local high-q scattering response changes with confinement and utilization. The present data do not distinguish among specific

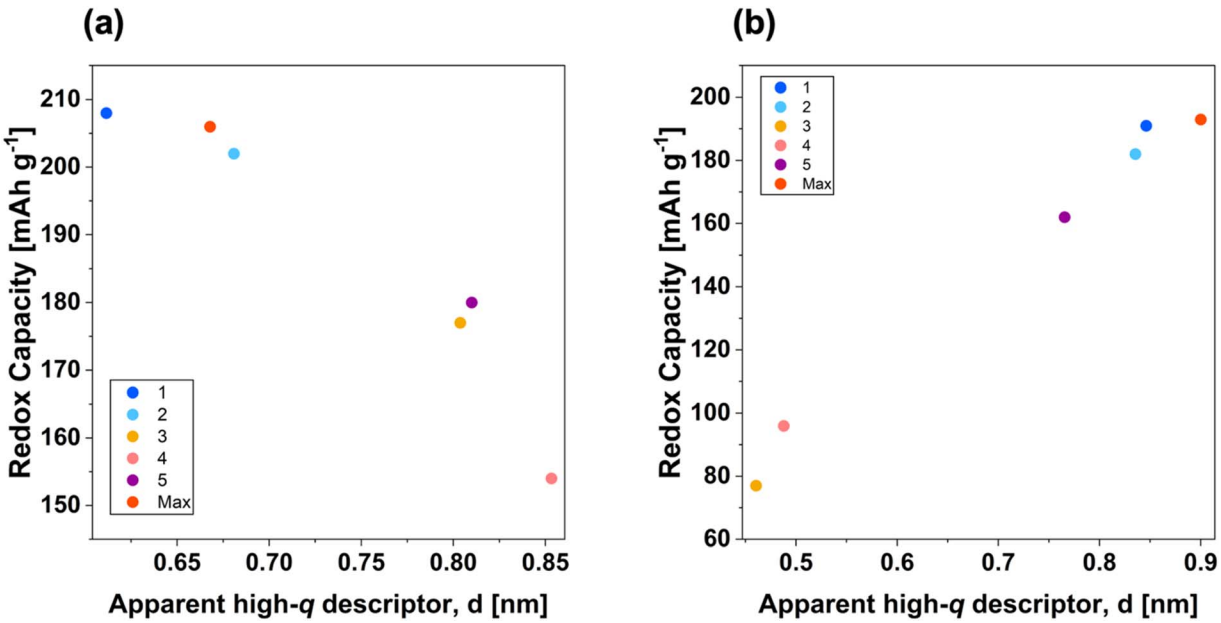

Fig. 3 Relationship between the Guinier-type-derived apparent descriptor *d* and redox capacity for (a) TCBQ and (b) DCAQ.

scenarios such as limited self-association, locally DCAQ-rich regions, or other sources of short-range contrast. Accordingly, we do not assign a specific packing motif (*e.g.*, π–π stacking)[19,46,47] or quantitative domain size on the basis of the present WAXS analysis alone, and such interpretations remain working hypotheses requiring independent validation by orthogonal structural methods.

Complementary roles of CO_2-PSD and high-*q* X-ray scattering analyses

Taken together, the robust structure–performance conclusions of this study are provided by the conductivity, CO_2-PSD, and electrochemical results. CO_2-PSD identifies the 0.7–0.8 nm micropores as the key storage window and clarifies the distinct accessibility constraints for TCBQ and DCAQ. The high-*q* WAXS parameterization adds only auxiliary information that the local high-*q* scattering response may differ between the two quinones once these primary accessibility/volume requirements are satisfied. We therefore use *d* only as a complementary, hypothesis-generating descriptor and not as independent structural proof.

These auxiliary WAXS observations may be broadly consistent with prior reports that local scattering contrast can be sensitive to confined-state organization in porous carbons.[48] However, in the present work, such information is used only in a secondary, hypothesis-generating manner. The robust design implications are instead derived from conductivity, pore accessibility, and the CO_2-PSD results, especially the availability of micropore volume within the 0.7–0.8 nm window.

Validation of device-level performance using beaker and pouch cells

Based on the principles established above, an optimized biomass-derived AC (sample 1) was selected for scalability validation. A two -electrode beaker cell utilizing sample 1 delivered gravimetric energy densities of 16.95 Wh kg^{-1} at ≈0.5C and 16.39 Wh kg^{-1} at ≈1C, as defined in the Experimental section (Fig. 4a). The cell exhibited an 80% capacity retention after 2000 high-rate cycles with a coulombic efficiency of ≈100% (Fig. 4b). This high performance in an idealized (beaker) format served as the benchmark for scalability.

Subsequently, a laminate-type pouch cell was fabricated (Fig. 5), as detailed in the Experimental section. The pouch cell employed thick-film electrodes with an areal mass loading of 13.9 mg cm^{-2} per side (27.8 mg cm^{-2} for both sides) of the anode and cathode, for a total of 56 mg cm^{-2} for the full cell. This places the device under practically relevant, high-loading conditions rather than the low-loading conditions typically used in fundamental studies. This cell achieved gravimetric energy densities of 17.3 Wh kg^{-1} at ≈0.1C and 12.9 Wh kg^{-1} at ≈1C (Fig. 6a). Compared with beaker-cell configurations, the energy density of pouch cells at ≈1C can be lower (≈20% in our system),[17,49] which we attribute to scale-up–related polarization sources rather than intrinsic limitations of the active materials. In general, thick-film porous electrodes can exhibit increased polarization at high current because larger thickness lengthens characteristic ion-transport pathways and enhances transport-related losses. In line with this expectation, our thickness-dependent Electrochemical Impedance Spectroscopy (EIS) (0.25–1.5 mm; Fig. S5) shows a nearly unchanged high-frequency intercept, while the mid-frequency arc becomes larger with thickness (can reflect increased effective interfacial and/or contact-related contributions, among other factors) and, more prominently, the low-frequency impedance increases strongly with thickness (rightward shift of Z'), suggesting enhanced transport-related polarization (*e.g.*, ionic transport resistance and concentration-related effects) in thicker electrodes. Such trends are commonly rationalized using porous-

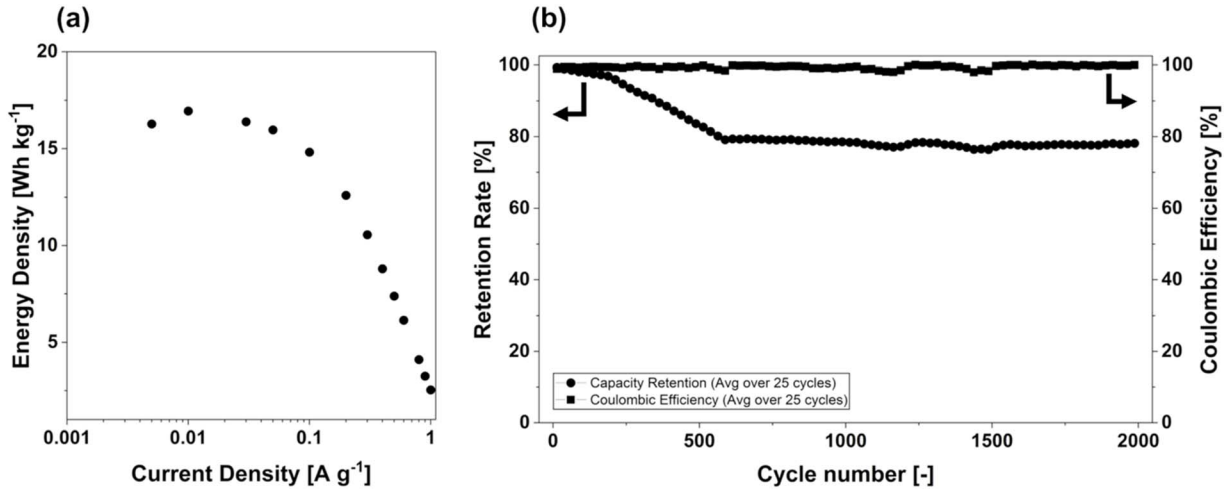

Fig. 4 Electrochemical performance of the beaker cell. (a) Rate capability at various current densities. (b) Cycling performance in terms of capacity retention (left axis) and coulombic efficiency (right axis) at 1 A g^{-1} for 2000 cycles. Each data point in (b) represents the average over 25 cycles.

electrode transmission-line frameworks, where distributed transport impedances become increasingly influential toward lower frequencies.[50,51] In this work, the single-sided electrode thicknesses are relatively close between the two configurations (beaker: ~0.45 mm single-sided; pouch: ~0.55 mm per side in a double-sided laminate with a total thickness of ~1.10 mm). Therefore, thickness-dependent transport polarization can explain part of the rate-related overpotential, but it is unlikely to be the only factor governing the larger performance loss in the pouch format. A major additional contribution can arise from current-collection/contact limitations and in-plane current distribution over the large electrode footprint. As the electrode footprint increases, the characteristic in-plane electronic path length along the current collector increases, which can generate in-plane potential gradients and current crowding near the tab and thereby amplify ohmic losses at higher currents.[52] Consistent with this mechanism, our pouch-cell comparison with and without a stainless-steel current-bus structure shows markedly reduced polarization already at 1C (smaller IR drop and a higher discharge–voltage profile) in the bus-integrated design (Fig. S6), supporting that current-collection/contact engineering is a key bottleneck for high-rate operation in large-area pouch cells. These results indicate that ion-transport and current-collection/contact engineering are key bottlenecks for high-rate, high-loading pouch-cell operation. In this system, however, the pouch cell delivered an energy density comparable to that of the beaker cell at 0.1C rate. This is significant because it demonstrates that the material-level design (*i.e.*, optimized micropore confinement) successfully preserves the inherent energy density upon scaling to a practical device format, at least at low rates. At 1C, the pouch cell retained ~79% of the energy density of the beaker cell (12.9 *vs.* 16.39 Wh kg^{-1}), indicating that high-rate performance remains limited by the engineering factors discussed below. Furthermore, the pouch cell exhibited exceptional durability, retaining 99.75% of its initial capacity after 3000 high-rate cycles with 100% coulombic efficiency (Fig. 6b). This cycle stability is among the highest reported for organic energy storage devices (Table 2).[31,53–56]

To contextualize this stability, a separate long-term soaking test on a beaker cell (an open system) confirmed the inherent dissolution tendency of the monomers, as detailed in the SI. The exceptional stability of the sealed pouch cell can therefore be attributed not only to micropore confinement but also to the optimized, low-electrolyte environment, which likely suppresses the dissolution–reprecipitation pathway.[15] This stability difference can be quantitatively rationalized by an electrolyte-volume-limited dissolution model, assuming that dissolution of the reduced species, tetrachlorohydroquinone (TCHQ), is the dominant mass-loss pathway. Using the aqueous solubility of TCHQ (76 mg L^{-1}) as a conservative upper bound,[18] we then calculated the maximum possible loss fraction based on the respective electrolyte volumes ($V \approx 120$ and 15 mL for the beaker and pouch cells, respectively) and initial TCBQ inventories (see Section S6 of the SI for detailed calculations). We note that in high-ionic strength electrolytes such as 0.5 M H_2SO_4, salting-out can further decrease the solubility of neutral organics; thus, the pure-water value intentionally represents a worst-case upper limit.[57] Accordingly, the present calculation provides a bounding estimate of the maximum possible loss rather than a quantitative prediction under acidic conditions.

To experimentally probe this dissolution pathway, combustion ion chromatography (CIC) was performed on electrolyte aliquots extracted from the beaker cells after 2000 cycles. The measured chlorine content directly reflects the concentration of dissolved chlorinated redox species, while the sulfur content verifies the supporting electrolyte composition. The average Cl concentration in the beaker electrolyte corresponds to a dissolved organic content consistent with the magnitude predicted by the volume-limited model (see Table S5). Notably, when the dissolved Cl is converted to an equivalent loss fraction under reasonable stoichiometric assumptions (*e.g.*, 1 : 1 dissolution of TCHQ and reduced DCAQ), the estimated capacity loss

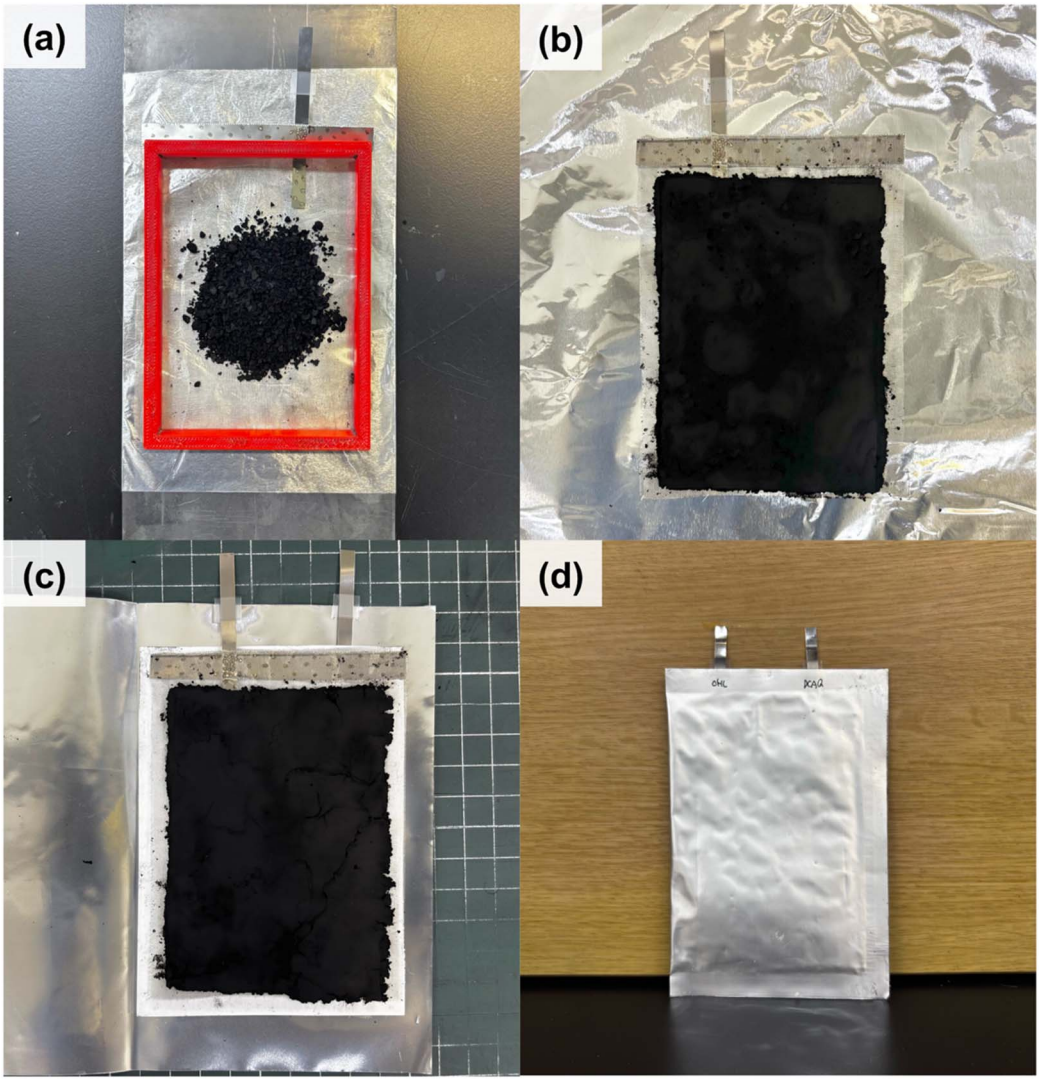

Fig. 5 Procedure for pouch cell fabrication. (a) Crushed quinone-impregnated composite pellets placed in a polylactic acid frame on the current collector. (b) Electrode after pressing. (c) Laminated stack of cathode, anode, and separator. (d) Final assembled pouch cell.

remains within the theoretical upper bound derived from solubility considerations.

The results showed that the maximum loss fraction for the beaker cell ($f_{max,beaker}$) is 28.3%, whereas that for the pouch cell ($f_{max,pouch}$) is 0.27%. Importantly, these calculated upper bounds align with the observed fade rates: the beaker cell lost ~23% over 2000 cycles (Fig. 4b), whereas the pouch cell lost only ~0.25% over 3000 cycles (Fig. 6b). In both cases, the observed fade is lower than the corresponding calculated maximum, supporting the hypothesis that capacity fade is constrained by the available electrolyte volume. The CIC results further corroborate that the extent of dissolved active species in the beaker system approaches, but does not exceed, the theoretical solubility limit, reinforcing electrolyte-volume control as the primary limiting factor under the present conditions.

This analysis quantitatively demonstrates that the sealed, low-electrolyte environment of the pouch cell is a critical factor in achieving exceptional cycle stability by severely constraining dissolution-based degradation. The adverse effect of an excessive amount of electrolyte on cycle stability provides an important insight into aqueous all-organic batteries and related organic-monomer-based cells, which generally suffer from poor long-term stability.

As a proof-of-concept demonstration, nine series-connected pouch cells were used to operate a tablet USB charging circuit, providing an open-circuit voltage of ≈6 V for the series stack. During charging, the voltage indicated on the DC–DC regulator module was ≈5.13 V (Fig. 6c). For the LED demonstration, five series-connected pouch cells were used to power a blue LED. This demonstration is qualitative, and continuous $V(t)$, $I(t)$, and $P(t)$ logging was not performed. This demonstration confirms that the material-level design principles are effective for driving practical loads. To further contextualize this demonstrated practical utility, the areal energy density of the pouch cell was evaluated. The device achieved an areal energy density of approximately 1 mWh cm^{-2} at 0.1C, which compares favorably with those of typical aqueous organic systems (≈0.3–0.8 mWh cm^{-2}) that generally employ much lower areal loadings in the 1–

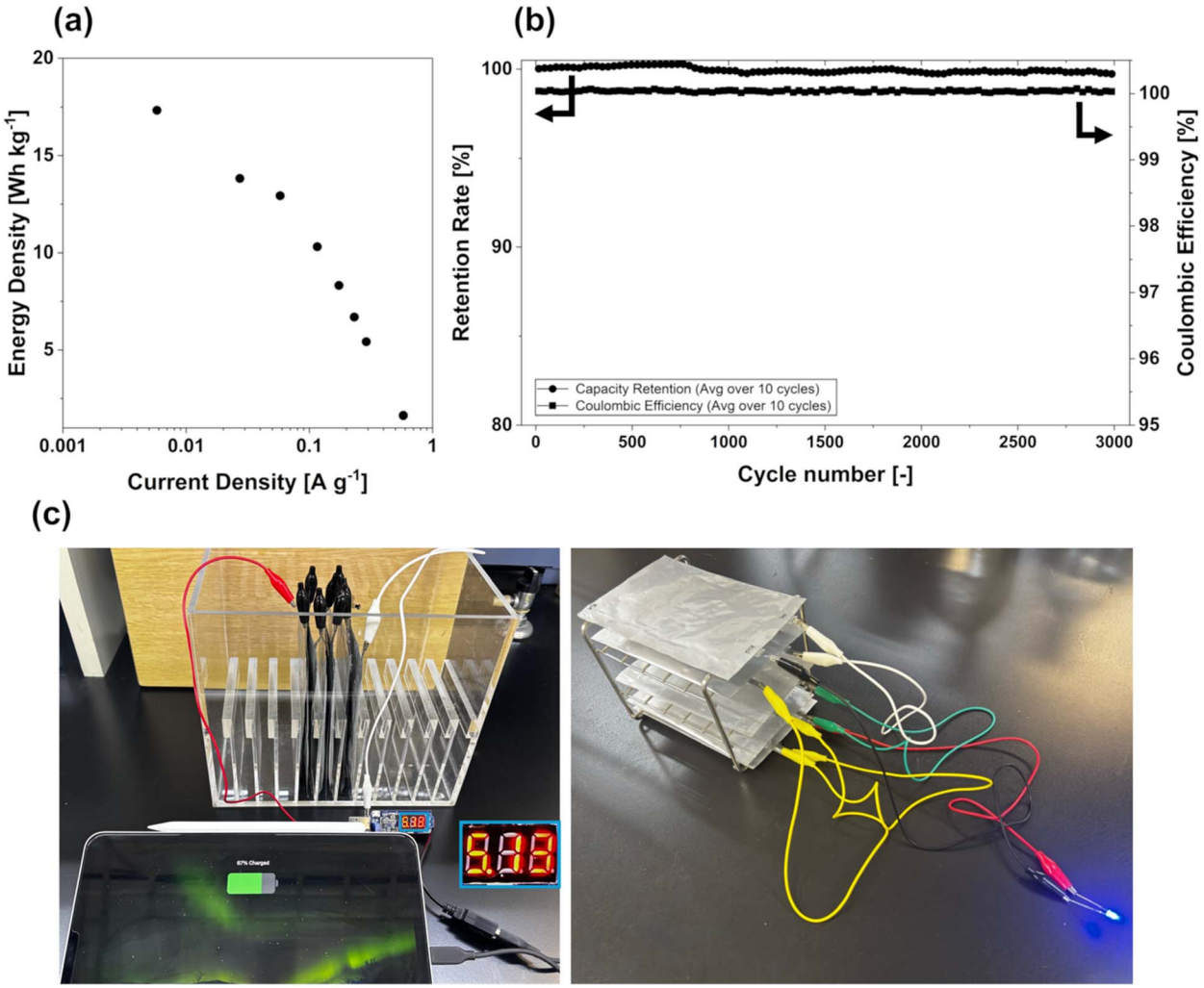

Fig. 6 Electrochemical performance and practical demonstration of the pouch cell. (a) Rate capability at various current densities. (b) Cycling performance in terms of capacity retention (left axis) and coulombic efficiency (right axis). Each data point is averaged over >10 cycles. (c) Photograph of two proof-of-concept demonstrations using series-connected pouch cells: nine cells connected in series (open-circuit voltage ≈6 V) operating a tablet USB charging circuit, with the output voltage indicated on the DC–DC voltage regulator module of ≈5.13 V, and five cells connected in series powering a blue LED.

10 mg cm^{-2} range.[17,20] This high areal energy density directly validates the thick-electrode design, with a combined active material loading of ∼55.6 mg cm^{-2} for the two electrodes, and is particularly significant because it is realized in a large-format cell (geometric area >60 cm^2) rather than a specialized small-area test configuration.

Taken together, the high areal energy density, gravimetric energy density of 17.3 Wh kg^{-1} at 0.1C, and exceptional long-term stability achieved *via* control of electrolyte-volume-limited dissolution in a large-format device collectively address the key implementation challenges for aqueous all-organic systems. This combination represents an important

Table 2 Comparison of electrochemical performance with state-of-the-art aqueous batteries

Ref.	System (anode‖cathode)	Electrolyte	Current density (A g^{-1})	Active-material loading	Cycle life
This work	Pouch cell, TCBQ‖DCAQ	0.5 M H_2SO_4	0.268	27.8 mg cm^{-2}	99.75% @ 3000
Small (2025)[56]	Coin cell, AQ‖DBBQ	2 M H_2SO_4	0.2	∼5.5 mg cm^{-2}	96% @ 330
Nat. Commun. (2024)[55]	Coin cell, PANI‖PANI	2m NaTFSI-PAE	0.147	1.5–2.6 mg cm^{-2}	92% @ 4800
Mater. Chem. Front. (2025)[31]	Coin cell, HATN‖2,6-DHN@CMK-3	9.5m H_3PO_4	10	∼2.0 mg cm^{-2}	∼70% @ 6000
Angew. Chem. (2024)[54]	Coin cell, TABQ‖TCBQ	0.5 M H_2SO_4	5	6.0–8.0 mg cm^{-2}	62.4% @ 5000
Appl. Surf. Sci. (2023)[53]	Coin cell AQ/C‖TCHQ/C	0.5 M $Al_2(SO_4)_3$	3	2.0–5.0 mg cm^{-2}	46.4% @ 1000

milestone toward the practical deployment of small-molecule organic electrodes.

Limitations and future outlook

This study demonstrated that our pore-structure-based design principles are transferable from the material level (beaker cells) to practical pouch cells. However, the pouch cell showed a significant performance drop at high discharge rates (Fig. 4a and 6a). This drop, evident as large overpotentials and rapid capacity fade at high currents, highlights scale-dependent engineering challenges that are not apparent in beaker cells.[17,58]

This observation aligns with recent developments in organic electrode research, where the primary bottleneck is increasingly shifting from the discovery of new redox chemistries to process development and cell engineering.[59] In practical, high-loading formats, intrinsic material properties are no longer the sole determinant of performance.

Recent work on pressurized organic electrodes exemplifies this shift.[60] In that study, performance gains arose partly from pressure-induced densification and enhanced π–π stacking within the organic phase—a mechanism distinct from our pore-structure-based control. Nevertheless, the same study concluded that at high mass loadings the dominant design levers shift to process-side parameters. These include stack pressure, electrode densification, and thick-electrode architecture. This convergence of conclusions underscores that mastering cell-level engineering is the next critical frontier in organic battery development.

First, effective stack pressure and its spatial uniformity are likely critical in pouch cells. Compared with small-area beaker cells, large-area pouch cells are more susceptible to nonuniform current distribution and contact-related polarization across the electrode plane. In thick electrodes, such scale-up can increase effective contact resistance at the electrode–current collector interface and within the electrode matrix, thereby causing larger IR drop and energy-density loss at high rates. Based on the present results and prior observations on electrode processing,[61] this suggests that press pressure, hot-rolling conditions (electrode density/porosity), and external compression are important design variables because they can reduce contact resistance while, if excessive, potentially restricting ionic pathways.

Second, current-collector/tab architecture is expected to become increasingly important at the pouch scale. Large electrode footprints and higher total currents can promote nonuniform in-plane current distribution (current crowding) and additional ohmic polarization; therefore, tab number/position and busbar- or mesh-type collector designs are likely important determinants of high-rate performance. Under otherwise identical electrode conditions, the influence of these factors would be reflected in rate-dependent IR drop and overpotential.[52] Polarization observed during high-rate operation can thus reasonably include both transport-related and contact/current-collection-related contributions.

Finally, electrode-scale design (thickness, porosity, and tortuosity) is critical in thick electrodes. For thick electrodes, rate performance becomes highly sensitive to ion transport distances and the tortuosity of the pore network. Even if the micropores (0.7–0.8 nm) are optimally matched to the dimensions of the quinone and the material possesses mesoporous networks (as in sample 1), high-rate performance will remain limited if electrode-scale diffusion resistances—governed by inter-particle porosity and tortuosity—dominate.[62] Studies on pressurized organic electrodes have demonstrated that high areal capacities and cycling stability are achievable in thick electrodes (0.5–1.6 mm, 50–150 mg cm^{-2}) under lean-electrolyte, low-N/P ratio (*i.e.*, a low negative-to-positive electrode capacity ratio), provided that macroporosity and tortuosity are co-optimized.[60] Therefore, future efforts must link our pore-level design rules to macroscopic descriptors such as tortuosity, compressive modulus, and binder/carbon distribution. A promising direction is the development of hierarchical pore architectures that combine fast ion transport pathways (inter-particle macropores) with intimate molecular-scale confinement provided by the optimized micropores.

In summary, the material design principles established here—sufficient electronic transport within the host carbon and availability of micropore volume within the 0.7–0.8 nm window—are valid and necessary at the cell scale. However, mechanical, interfacial, and electrode-scale engineering factors are currently the bottlenecks in achieving high-rate pouch cell performance. Systematically addressing stack pressure management, current collector architecture, and thick-electrode design, informed by recent process engineering strategies,[32,59] will be the key to unlocking the full potential of this material system and translating the high performance of beaker cells into practical high-loading pouch cells.

Conclusions

In this work, we established molecule-specific design principles for biomass-derived ACs hosting LMW quinones in aqueous rocking-chair-type all-organic proton cells. By systematically analyzing the relationship between the electrochemical performance of TCBQ and DCAQ and the physicochemical properties of a diverse set of commercial ACs, we identified sufficient electronic conductivity as a key prerequisite for redox activity. Beyond this prerequisite, pore accessibility was identified as a dominant factor influencing the effective utilization of active materials. While the compact TCBQ molecule demonstrated resilience in various pore structures, its utilization was facilitated by the mesopore network, showing partial suppression in hosts where diffusion paths were restricted. In contrast, the larger DCAQ molecule suffered drastic capacity loss in low-surface-area carbons, indicative of a molecular sieving effect where constricted pore entrances can restrict molecular access to the active species. This indicates that sufficient specific surface area is an important requirement for DCAQ to access electrochemically active sites.

For hosts satisfying these accessibility requirements, PSD analysis revealed that the pore volume in a very narrow diameter window (0.7–0.8 nm) strongly correlates with the redox capacity. This corroborates the importance of matching subnanometer

geometric confinement with the molecular dimensions of the active species. Furthermore, high-q WAXS parameterization provided only supplementary, hypothesis-generating information on short-range scattering differences after the primary accessibility and volume effects had been established by CO_2-PSD. For TCBQ, d showed no simple relationship with capacity and was not used as a predictive variable. For DCAQ, a positive within-dataset association between capacity and the apparent descriptor d was observed, consistent with but not proving changes in local association/packing under confinement. Accordingly, the robust design conclusions of this work rest on conductivity, pore accessibility, and the 0.7–0.8 nm micropore volume, whereas the high-q analysis is presented as complementary evidence requiring future validation. Guided by these design principles, we selected an optimized biomass-derived AC (sample 1), which features both the mesoporous ionic highways required for TCBQ kinetics and the maximal 0.7–0.8 nm micropore volume for DCAQ capacity. Using this host, we successfully translated the material-level insights into a practical, high-loading laminate-type pouch cell. The resulting device, employing thick-film electrodes with an areal active material loading of $\approx$28 mg cm^{-2} and areal energy density of $\approx$1 mWh cm^{-2}, delivered gravimetric densities of 17.3 Wh kg^{-1} at 0.1C and 12.9 Wh kg^{-1} at 1C, while retaining 99.75% of its capacity after 3000 high-rate cycles.

Quantitative analysis based on an electrolyte-volume-limited dissolution model supports that the combination of nanoscale micropore confinement and a sealed, low-electrolyte pouch configuration can substantially mitigate dissolution-driven degradation, thereby enabling an extremely low capacity fade of $\sim$0.25% over 3000 cycles ($\approx$99.75% retention). Taken together, this study demonstrates that rational, molecule-specific micropore engineering of biomass-derived ACs can bridge nanometer-scale confinement phenomena with device-level performance, providing a potentially general framework for the development of durable, high-loading, aqueous all-organic energy storage systems. More broadly, the present results suggest potential applicability of this pouch-cell concept to larger-format implementations and to operation under practical load conditions relevant to renewable-energy storage.

Experimental

Materials preparation

Quinones (TCBQ and DCAQ) were purchased from Tokyo Chemical Industry Co., Ltd. Petroleum-coke-derived AC (Maxsorb®) was purchased from Kansai Coke & Chemicals Co., Ltd. Seven commercially available biomass-derived AC were used in this study, and their precursor types and activation method are summarized in Table 1. All reagents were used as received without further purification.

Impregnation of the AC with quinone followed our previous protocol:[51] TCBQ (3.0 g) or DCAQ (3.0 g) was dissolved in acetone (1.5 L for TCBQ, 3.0 L for DCAQ) with sonication (10 min). Subsequently, AC (7.0 g) was added and dispersed by sonication (1 h). The suspension was stirred at 80 °C to evaporate acetone, allowing quinone molecules to impregnate the nanopores. The obtained powder was gently dried on a hot plate stirrer at 80 °C for 12 h in air, gently ground, and mixed in an agate mortar. The final quinone loading was quantified by combustion ion chromatography (HIC-20Asp, Shimadzu) to confirm successful impregnation. The measured organic chlorine content (Cl wt%) was converted to quinone loading by stoichiometry (see the SI for conversion factors). For both the TCBQ and DCAQ systems, the impregnated carbon was prepared using a fixed internal quinone:AC ratio of 27 : 63 (corresponding to 30 wt% quinone). Based on this baseline, electrode solids for each cell configuration were blended. The ratios of the conductive additive (carbon black) and polytetrafluoroethylene (PTFE) binder (6-J, Mitsui-DuPont Fluorochemicals) were individually optimized to maximize electrochemical performance and mechanical integrity for each cell format. The compositions (quinone : AC : carbon black : PTFE) are as follows (ratios are parts by mass and normalized to 100): (i) half-cell (beaker, three-electrode), 27 : 63 : 0 : 10; (ii) beaker-scale cell (two-electrode), 27 : 63 : 5 : 5; (iii) pouch cell (cathode, TCBQ), 24.6 : 57.4 : 8 : 10; and (iv) pouch cell (anode, DCAQ), 26.1 : 60.9 : 8 : 5.

Physicochemical characterization

Electronic conductivity. The electronic conductivities of the pristine (unimpregnated) AC powders (AC : PTFE = 98 : 2) were measured at room temperature using the four-point probe method (Loresta-FX MCP-T380, Nittoseiko Analytech) under applied pressure.

N2 adsorption–desorption (77 K). N_2 adsorption–desorption isotherms at 77 K were measured using a QuadraSorb Station 3 analyzer (Quantachrome Instruments) after degassing at 130 °C for 4 h under vacuum. SSAs were calculated using the Brunauer–Emmett–Teller (BET) method. Mesopore size distributions and mesopore volumes were derived from the desorption branch using the Barrett–Joyner–Halenda (BJH) method. Cumulative pore volumes were read at $P/P_0 = 0.99$.

CO2 adsorption (273 K). CO_2 adsorption isotherms at 273 K were measured using a QuadraSorb Station 1 analyzer (Quantachrome Instruments) after the same degassing protocol as above (130 °C, 4 h, vacuum). The PSD was derived from the CO_2 adsorption isotherm using a non-local DFT model provided by the instrument software. This analysis allowed the quantification of the specific pore volume within the 0.7–0.8 nm window, which was used for the correlations presented in the Results and discussion section.

X-ray scattering. SAXS/WAXS measurements were performed on the TCBQ/DCAQ-impregnated powder specimens (samples 1–5 and Maxsorb®) at the NanoTerasu synchrotron radiation facility (BL08W beamline). The high-q region (WAXS) was additionally analyzed to compare differences in the short-range scattering response among samples. High-q WAXS profiles were parameterized by a Guinier-type linearization to generate an apparent descriptor d of the profile shape. Because a strict Guinier regime could not be established, d is used only for internal comparison among samples analyzed with the same protocol and is not interpreted as an absolute structural length

scale. The detailed fitting parameters, q-ranges, and formal conversion from R_{app} to d are provided in Section S7 of the SI.

Combustion ion chromatography. Chlorine (Cl) and sulfur (S) contents in the electrolyte were quantified by combustion ion chromatography (YHS-11, Yanaco). Electrolyte aliquots collected after cycling were weighed (several milligrams) and absorbed onto ash-free filter paper, wrapped in aluminum foil, and introduced into the combustion unit. Combustion was conducted at 950 °C for 16 min under purified air. The resulting combustion gases were absorbed and analyzed by ion chromatography to determine Cl^- and SO_4^{2-} concentrations. The reported elemental contents (wt%) are referenced to the initial mass of the electrolyte solution.

Fabrication of a single beaker cell and pouch cell. Electrodes were fabricated using the direct powder adhesion (DPA) method, a solvent-free process that enables the rapid production of high-mass-loading electrodes suitable for roll-to-roll processing. The procedure was based on a previously reported protocol.[61]

The resulting powder was used to fabricate the various cell configurations detailed below. In all full cells, the TCBQ-based electrode served as the cathode and the DCAQ-based electrode served as the anode. Following assembly, all cells were degassed under reduced pressure until no visible gas bubbles remained to displace trapped air and drive the electrolyte into the micro/mesoporous network of the electrodes and separator to ensure complete wetting.

Half-cell (beaker, three-electrode). The quinone-impregnated composite pellet was deposited onto a 2.0 × 2.0 cm frame on an Au mesh current collector, pressed at a nominal pressure of ~75 MPa, calculated from the applied load and the 20 × 20 mm spacer contact area, and then trimmed. Cells were assembled using a DPA sheet on an Au mesh as the working electrode, Ag/AgCl reference (3 M KCl aq.), polypropylene separator (Nippon Kodoshi Co.), and 0.5 M H_2SO_4 aqueous electrolyte. The counter electrode was an AC sheet with a formulation of AC : PTFE = 9 : 1, prepared on a mesh and used in an excess amount greater than five times the mass of the working electrode.

Beaker-scale cell (two-electrode). Cathode (TCBQ) and anode (DCAQ) DPA sheets were prepared on an SUS316 mesh using a 2.0 × 2.0 cm frame, pressed at 30 kN, and then trimmed to the target footprint. Prior to assembly, the TCBQ electrodes were electrochemically pre-reduced to tetrachloro-1,4-hydroquinone in a beaker half-cell at approximately 1.0–1.3C. Two-electrode beaker cells with a polypropylene separator and 0.5 M H_2SO_4 aqueous electrolyte were assembled. The typical areal mass loading was 34.5 mg cm^{-2} per electrode.

Pouch full cell. Cathode (TCBQ) and anode (DCAQ) composites were prepared on an SUS316 mesh using a 9.5 × 7.0 cm frame and pressed at 45 kN. After pressing, each adhered sheet was calendered with a heated roll at 40 °C to a nominal thickness of 1.10 mm to homogenize thickness and improve interfacial contact. This target thickness was chosen based on a practical-scale quinone-based device study that systematically optimized single-sided electrode thickness (0.5–1.5 mm), where ~0.5 mm per side offered superior rate performance; thus, we adopted a double-sided configuration (~0.5 mm per side) in the present pouch cell.[17] An SUS316 bus plate with a width of 8 mm was spot-welded along the top edge of each mesh to increase the cross-section of the current bus bar and reduce in-plane resistance. Prior to assembly, the TCBQ electrodes were electrochemically pre-reduced to TCHQ in a beaker half-cell at approximately 1.0–1.3C. Electrode pairs of identical geometric area were stacked with a polypropylene separator and placed in an Al laminate pouch, filled with 0.5 M H_2SO_4 (15 mL), evacuated (to approximately 98.5% vacuum) to impregnate the porous electrodes, and heat-sealed. The typical areal mass loading was 13.9 mg cm^{-2} per side.

Electrochemical tests. Electrochemical measurements were performed at 25 °C using a potentiostat (Vertex, Ivium Technologies). Voltage windows were set as follows: 0.0–1.0 V *vs.* Ag/AgCl for TCBQ half-cells; −0.2–0.2 V *vs.* Ag/AgCl for DCAQ half-cells; and 0.0–1.2 V (terminal cell voltage) for full cells (beaker and pouch).

C-rates were defined differently for the half-cell and full-cell configurations. For the half-cells, the current (I) was normalized by the mass of the active material in the working electrode (m_{active}) and its corresponding theoretical capacity (218 mA h g^{-1} for TCBQ; 194 mA h g^{-1} for DCAQ). For the full cells (beaker and pouch), the current (I) was defined solely by the mass of TCBQ in the cathode (m_{TCBQ}) and its theoretical capacity: $I = C \times 218$ (mAh g^{-1}) × m_{TCBQ}.

Electrochemical impedance spectroscopy (EIS) measurements were also conducted using the same potentiostat (Vertex, Ivium Technologies). EIS was performed in a three-electrode half-cell configuration at room temperature with an Ag/AgCl reference electrode. The counter electrode was an AC sheet with a formulation of AC : PTFE = 9 : 1, prepared on a mesh and used in an excess amount greater than five times the mass of the working electrode. Impedance spectra were collected over a frequency range of 20 000–0.1 Hz (30 logarithmically spaced frequency points) with a sinusoidal perturbation amplitude of 100 mV. TCBQ-impregnated working electrodes with different film thicknesses (0.25, 0.5, 1.0, and 1.5 mm) were evaluated.

Calculation of performance metrics. The energy density (Wh kg^{-1}) was determined from the galvanostatic discharge curve. The discharge energy (E) was obtained by integrating the product of voltage and current over time and normalizing it by the total mass of the pressed electrode composites on both electrodes ($m_{total\ electrodes}$), including the active material, carbon host, conductive additive, and binder.

The capacity retention (R_n) was calculated as the discharge capacity of a given cycle (Q_n) divided by the discharge capacity of the first cycle (Q_1), expressed as a percentage: $R_n = (Q_n/Q_1) \times 100\%$.

Author contributions

K. R.: writing – original draft, visualization, validation, methodology, investigation, formal analysis, data curation. N. H.: methodology, investigation, formal analysis, data curation. R. K.: investigation, validation. A. K.: validation. T. Y.: formal analysis, data curation. Y. K.: methodology, validation. M. W.:

writing – review & editing, resources. K. K.: methodology, investigation, formal analysis, data curation. Y. N.: writing – review & editing, visualization, validation, supervision, resources, project administration, methodology, funding acquisition, conceptualization.

Conflicts of interest

This study was partly conducted under a collaboration with Satoyama Engineering Co., Ltd. The authors declare no personal financial interests. Y. N. serves as a board member of Satoyama Engineering Co., Ltd, which provided collaborative research funding for this work. This relationship has been appropriately managed and does not affect the objectivity of this study.

Data availability

The data supporting this article have been included as part of the supplementary information (SI). Supplementary information: additional galvanostatic charge–discharge and combustion ion chromatography data, CO_2 adsorption-derived micropore size distributions, detailed DFT-derived molecular dimensions of TCBQ and DCAQ, thickness-dependent EIS and current-collector architecture effects in pouch cells, high-q WAXS parameterization of apparent profile descriptors, and electrolyte-volume-limited dissolution analyses including N_2-bubbling experiments. See DOI: https://doi.org/10.1039/d5ta10161a.

Acknowledgements

The authors also thank Satoyama Engineering Co., Ltd for providing collaborative research funding that partially supported this work. This work was also supported by the Japan Society for the Promotion of Science (JSPS) KAKENHI (grant number 24K01243); Environment Research and Technology Development Fund (grant number JPMEERF20223C04) from the Environmental Restoration and Conservation Agency, Ministry of the Environment of Japan; and Tohoku Initiative for Fostering Global Researchers for Interdisciplinary Sciences (TI-FRIS) under the Strategic Professional Development Program for Young Researchers of the Ministry of Education, Culture, Sports, Science and Technology (MEXT). The authors also acknowledge the generous support from FRIS CoRE, Tohoku University, a shared research facility. The synchrotron radiation experiments in this study were conducted at the NanoTerasu BL08W-WAXS beamline under the Tohoku University NanoTerasu Strategic Utilization Promotion Support System.The authors gratefully acknowledge Kuraray Co., Ltd for the generous provision of samples used in this work. We would like to thank Editage (https://www.editage.jp) for English language editing. This work utilized AI-based tools to assist with language editing and manuscript preparation. The authors take full responsibility for the content of the manuscript.

Notes and references

1 N. Armaroli and V. Balzani, *Angew. Chem., Int. Ed.*, 2007, **46**, 52–66.
2 B. Dunn, H. Kamath and J.-M. Tarascon, *Science*, 2011, **334**, 928–935.
3 E. Fan, L. Li, Z. Wang, J. Lin, Y. Huang, Y. Yao, R. Chen and F. Wu, *Chem. Rev.*, 2020, **120**, 7020–7063.
4 J. Winsberg, T. Hagemann, T. Janoschka, M. D. Hager and U. S. Schubert, *Angew. Chem., Int. Ed.*, 2017, **56**, 686–711.
5 D. Xu, M. Liang, S. Qi, W. Sun, L.-P. Lv, F.-H. Du, B. Wang, S. Chen, Y. Wang and Y. Yu, *ACS Nano*, 2021, **15**, 47–80.
6 M. Yin, X. Zhou and Z. Xue, *Macromol. Chem. Phys.*, 2024, **225**, 2300427.
7 F. Sprang and S. R. Waldvogel, *ACS Electrochem.*, 2025, **1**, 25–35.
8 B. Huskinson, M. P. Marshak, C. Suh, S. Er, M. R. Gerhardt, C. J. Galvin, X. Chen, A. Aspuru-Guzik, R. G. Gordon and M. J. Aziz, *Nature*, 2014, **505**, 195–198.
9 G. Di Florio, I. Pucher, P. Todeschi, M. C. Baratto, R. Basosi and E. Busi, *J. Cleaner Prod.*, 2022, **343**, 130899.
10 H. Wang, R. Emanuelsson, A. Banerjee, R. Ahuja, M. Strømme and M. Sjödin, *J. Phys. Chem. C*, 2020, **124**, 13609–13617.
11 Q. Zhao, Z. Zhu and J. Chen, *Adv. Mater.*, 2017, **29**, 1607007.
12 S. P. Ega and P. Srinivasan, *J. Energy Storage*, 2022, **47**, 103700.
13 S. Bi, S. Wang, F. Yue, Z. Tie and Z. Niu, *Nat. Commun.*, 2021, **12**, 6991.
14 S. Wang, Q. Guo, H. Liu, L. Zhang, C. Zhang, T. Zhou, Q. Ma, H. Li, R. Wang and Y. Zheng, *Chem. Sci.*, 2024, **15**, 1051–1060.
15 T. Tomai, H. Hyodo, D. Komatsu and I. Honma, *J. Phys. Chem. C*, 2018, **122**, 2461–2466.
16 Y. Katsuyama, Y. Nakayasu, K. Oizumi, Y. Fujihara, H. Kobayashi and I. Honma, *Adv. Sustainable Syst.*, 2019, **3**, 1900083.
17 Y. Katsuyama, T. Takehi, S. Sokabe, M. Tanaka, M. Ishizawa, H. Abe, M. Watanabe, I. Honma and Y. Nakayasu, *Sci. Rep.*, 2022, **12**, 3915.
18 T. Tomai, S. Mitani, D. Komatsu, Y. Kawaguchi and I. Honma, *Sci. Rep.*, 2014, **4**, 3591.
19 D. Takimoto, K. Suzuki, R. Futamura, T. Iiyama, S. Hideshima and W. Sugimoto, *ACS Appl. Mater. Interfaces*, 2022, **14**, 31131–31139.
20 D. R. Lobato-Peralta, P. U. Okoye and C. Alegre, *J. Power Sources*, 2024, **617**, 235140.
21 K. C. S. Lakshmi and B. Vedhanarayanan, *Batteries*, 2023, **9**, 202.
22 Q. Wang, B. Luo, Z. Wang, Y. Hu and M. Du, *Molecules*, 2024, **29**, 5172.
23 N. Arena, J. Lee and R. Clift, *J. Cleaner Prod.*, 2016, **125**, 68–77.
24 J. Saleem, Z. K. B. Moghal, F. Tahir, T. Al-Ansari and G. McKay, *C*, 2025, **11**, 22.

25 A. Vilén, P. Laurell and R. Vahala, *J. Environ. Manage.*, 2022, **324**, 116356.
26 Y. Nakayasu, S. Sokabe, Y. Hiraga and M. Watanabe, *Chem. Commun.*, 2023, **59**, 3079–3082.
27 K. Nueangnoraj, T. Tomai, H. Nishihara, T. Kyotani and I. Honma, *Carbon*, 2016, **107**, 831–836.
28 J.-H. Kim, S.-C. Jung, H.-M. Lee and B.-J. Kim, *Int. J. Mol. Sci.*, 2022, **23**, 3680.
29 H. Itoi, S. Tazawa, H. Hasegawa, Y. Tanabe, H. Iwata and Y. Ohzawa, *RSC Adv.*, 2019, **9**, 27602–27614.
30 Y. Nakayasu, S. Sokabe, N. Nagamura, C. Ooka, T. Yamada, K. Kobayashi and M. Watanabe, *ACS Appl. Mater. Interfaces*, 2026, **18**(10), 14947–14959.
31 Q. Xu, L. Liu, K. Chen, Y. Xiang, X. Liu, H. Yu, L. Zhang, L. Yan and J. Shu, *Mater. Chem. Front.*, 2025, **9**, 3264–3273.
32 J. Li and H. Liang, *Energy Mater.*, 2024, **4**, 400033.
33 J. Chmiola, G. Yushin, Y. Gogotsi, C. Portet, P. Simon and P. L. Taberna, *Science*, 2006, **313**, 1760–1763.
34 X. Yin, S. Sarkar, S. Shi, Q.-A. Huang, H. Zhao, L. Yan, Y. Zhao and J. Zhang, *Adv. Funct. Mater.*, 2020, **30**, 1908445.
35 D. Komatsu, T. Tomai and I. Honma, *J. Power Sources*, 2015, **274**, 412–416.
36 E. Raymundo-Piñero, K. Kierzek, J. Machnikowski and F. Béguin, *Carbon*, 2006, **44**, 2498–2507.
37 P. Simon and Y. Gogotsi, *Nat. Mater.*, 2008, **7**, 845–854.
38 C. Largeot, C. Portet, J. Chmiola, P.-L. Taberna, Y. Gogotsi and P. Simon, *J. Am. Chem. Soc.*, 2008, **130**, 2730–2731.
39 L. Zhang and S. Zuo, *Molecules*, 2024, **29**, 3197.
40 T. Mi, L. Chen, S. Xin and X. Yu, *J. Nanomater.*, 2015, **2015**, 910467.
41 Z. Yang, Y. Bao, H. Xu, M. Liu and Y. Chen, *Electrochim. Acta*, 2025, **541**, 147281.
42 D. Takimoto, K. Suzuki, S. Hideshima and W. Sugimoto, *Electrochemistry*, 2023, **91**, 077006.
43 M. Liu, H. Xu, Y. Bao and Y. Chen, *J. Energy Storage*, 2025, **116**, 116110.
44 Y. Liu, M. Paskevicius, M. V. Sofianos, G. Parkinson, S. Wang and C.-Z. Li, *Fuel*, 2021, **292**, 120384.
45 L. Boldon, F. Laliberte and L. Liu, *Nano Rev.*, 2015, **6**, 25661.
46 C. Kitamura, N. Akamatsu, A. Yoneda and T. Kawase, *Acta Crystallogr., Sect. E:Crystallogr. Commun.*, 2008, **64**, o1802.
47 C. Kitamura, N. Kawatsuki and A. Yoneda, *Anal. Sci.:X-Ray Struct. Anal. Online*, 2006, **22**, x293–x294.
48 C. Prehal, D. Weingarth, E. Perre, R. T. Lechner, H. Amenitsch, O. Paris and V. Presser, *Energy Environ. Sci.*, 2015, **8**, 1725–1735.
49 B. K. Chakrabarti and C. T. J. Low, *Next Energy*, 2024, **4**, 100137.
50 J. Moškon and M. Gaberšček, *J. Power Sources Adv.*, 2021, **7**, 100047.
51 A. Ch. Lazanas and M. I. Prodromidis, *ACS Meas. Sci. Au*, 2023, **3**, 162–193.
52 W. Zhao, G. Luo and C.-Y. Wang, *J. Power Sources*, 2014, **257**, 70–79.
53 T. Sun, J. Yang, H. Peng, F. Kang, J. Zhang and Q. Zhang, *Small*, 2025, **21**, 2502591.
54 Y. Su, H. Jiang, Q. Kang, X. Meng, X. Zheng, J. Lu, X. Mei, X. Sun, L. Yan and T. Ma, *Appl. Surf. Sci.*, 2023, **625**, 157174.
55 S. Wu, M. Taylor, H. Guo, S. Wang, C. Han, J. Vongsvivut, Q. Meyer, Q. Sun, J. Ho and C. Zhao, *Angew. Chem., Int. Ed.*, 2024, **63**, e202412455.
56 Y. Hong, K. Jia, Y. Zhang, Z. Li, J. Jia, J. Chen, Q. Liang, H. Sun, Q. Gao, D. Zhou, R. Li, X. Dong, X. Fan and S. He, *Nat. Commun.*, 2024, **15**, 9539.
57 W.-H. Xie, W.-Y. Shiu and D. Mackay, *Mar. Environ. Res.*, 1997, **44**, 429–444.
58 V. Augustyn, P. Simon and B. Dunn, *Energy Environ. Sci.*, 2014, **7**, 1597–1614.
59 J. Bitenc, K. Pirnat, O. Lužanin and R. Dominko, *Chem. Mater.*, 2024, **36**, 1025–1040.
60 Z. Xu, Y. Xu, Y. Qiu, Y. Cao, S. Gasilov, G. Li, J. Lu and X. Wang, *Nat. Commun.*, 2025, **16**, 4561.
61 N. Haba, Y. Katsuyama, A. Kido, K. Morimoto and Y. Nakayasu, *Batteries Supercaps*, 2025, **8**, e202400721.
62 J. Zheng, G. Xing, L. Jin, Y. Lu, N. Qin, S. Gao and J. P. Zheng, *Batteries*, 2023, **9**, 151.

